Journal Name

ARTICLE TYPE

Cite this: DOI: 10.1039/xxxxxxxxxx

Morphology of viscoplastic drop impact on viscoplastic surfaces

Simeng Chen and Volfango Bertola*

Received Date
Accepted Date

DOI: 10.1039/xxxxxxxxxx

www.rsc.org/journalname

The impact of viscoplastic drops onto viscoplastic substrates characterized by different magnitudes of the yield stress is investigated experimentally. The interaction between viscoplastic drops and surfaces has an important application in additive manufacturing, where a fresh layer of material is deposited on a partially cured or dried layer of the same material. So far, no systematic studies on this subject have been reported in literature. The impact morphology of different drop/substrate combinations, with yield stresses ranging from 1.13 Pa to 11.7 Pa, was studied by high speed imaging for impact Weber numbers between 15 and 85. Experimental data were compared with one of the existing models for Newtonian drop impact onto liquid surfaces. Results show the magnitude of the yield stress of drop/substrate strongly affects the final shape of the impacting drop, permanently deformed at the end of impact. The comparison between experimental data and model predictions suggests the crater evolution model is only valid when predicting the evolution of the crater at sufficiently high Weber numbers.

1 Introduction

Viscoplastic fluids are an important type of non-Newtonian fluids, which respond like an elastic solid when the applied stress is below a threshold value (called the yield stress), and start to flow when the yield stress is overcome. In practice, many soft materials in industrial or everyday products exhibit such property, including slurries and suspensions, crystallizing lavas, some polymer solutions, muds and clays, heavy oils, cosmetic creams, hair gel, liquid chocolate, and toothpaste[1,2]. Due to this special property viscoplastic fluids have important applications in various fields ranging from the oil and chemical industries, to food processing, cosmetics, and geophysical fluid dynamics. Currently, there is a growing interest in studying the behaviour of viscoplastic fluids in the drop-on-demand process[3–6] because it is relevant to additive manufacturing (3D printing). Consequently a better understanding of the mechanism of viscoplastic drop formation and its interaction with target surfaces is necessary.

Besides their numerous applications in industry, viscoplastic fluids have also attracted much academic interest in recent years. The literature has shown that the formation of a viscoplastic drop from a capillary nozzle and the interactions between the viscoplastic drops and solid surfaces are significantly affected by the magnitude of the yield stress[4,7–10]. These phenomena, where both the fluid yield stress and surface tension are important, can be often characterised in terms of the Bingham-capillary number, $B = \tau_0 D_0/\sigma$, where τ_0 is the yield stress and σ the surface tension, which compares the yield stress and the Laplace pressure[11]. Spreading of viscoplastic drops (Carbopol solutions) over treated/ untreated glass surfaces were experimentally investigated using a confocal microscopy system and the apparent slip was observed by measuring the vertical profile of radial velocity over untreated surface[12]. The impact of yield stress fluid drops on horizontal surfaces coated with a layer of the same material was studied experimentally[13]; in this study, impact events were categorized and a single dimensionless parameter was introduced to reduce the impact regime map. The deformation and breakup of coal-water slurry drops (characterised by Bingham viscoplastic model) in a continuous air jet were studied using numerical simulation and the results show good predictions for the breakup regimes[14]. The encapsulation of droplets within a viscoplastic fluid for the purpose of transportation was explored both analytically and computationally and it was found that the stability of

* *Laboratory of Technical Physics, School of Engineering, University of Liverpool, The Quadrangle, Brownlow Hill L69 3GH, United Kingdom. E-mail: Volfango.Bertola@liverpool.ac.uk*

the encapsulated droplets was governed by the length scale of the flow and yield stress of the encapsulating fluid[15]. More recently a lattice Boltzmann model was used to simulate multiphase viscoplastic fluid flow[16]. Good agreements between the simulation results and the corresponding theoretical solutions were obtained for different cases, including droplet(s) falling and interaction in Bingham fluid, and sessile viscoplastic droplet motion.

The interactions between impacting drops and liquid layers are related to various engineering applications, ranging from secondary atomization by collision with a wall, spray deposition, coating to spray cooling. In these applications, the crater formation by drop impact plays an important role because of its relation to several basic impacting outcomes (e.g. maximum spreading, penetration depth, splashing behaviour etc.). It was found that deep liquid splashing was determined by both the Froude and the Weber numbers, while shallow liquid splashing was determined essentially by the Weber number. The impact of a water drop onto a water surface was experimentally studied trough high-speed imaging in[17]. A map showing different regimes of cavity and impact drop behaviour based on Weber and Froude numbers was constructed. The impact of a drop on liquid surface (water & aqueous glycerol solution) was studied experimentally and theoretically in the region of the fully developed splashing[18]. A theoretical model for crater evolution was presented and it was shown that the maximum crater radius and the crater collapse time depend on both the Froude number and the dimensionless capillary length. The amount of entrained air during the impact of a drop/solid sphere on to a deep liquid pool was investigated numerically by Hendrix et al[19]. The results were compared with various experimental data and excellent agreement was found.

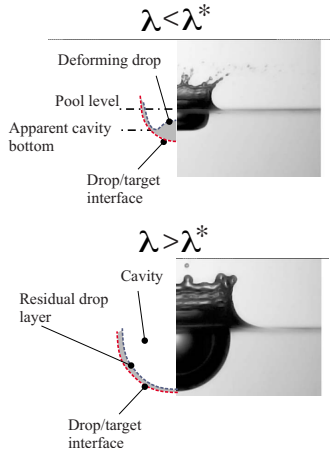

Fig. 1 Phases of crater evolution. (Adapted from[20])

More recent works investigated the effect of the liquid pool depth[21] and of the impingement angle[22], while others analysed the coalescence process of droplets impacting on polymeric liquid layers[23]. Recently, an experimental and theoretical investigation on the crater formed by impact of a single drop onto a semi-infinite target of the same liquid led to a theoretical model which is able to predict the temporal variation of crater depth for various impact parameters[20]. Generally, the whole process of crater evolution is divided into two phases, illustrated in Figure 1 (note dimensionless time $\lambda = u_i t/D_0$, is used here). During the first stage ($\lambda < \lambda^*$), the material interface between the drop and the substrate is not visible and the penetration velocity of the crater is $0.44u_i$, which was derived from a modified quasistationary model of initial drop penetration. Thus, the dimensionless crater depth, Δ, grows linearly with respect to the dimensionless time: $\Delta = 0.44\lambda$. During the second phase ($\lambda > \lambda^*$), the shape of the crater can be well approximated by the shape of the drop/target interface due to a very thin residual liquid layer of the drop material on the crater surface. The evolution of the crater was obtained from the balance of stresses at the crater interface, accounting for inertia, gravity, and surface tension. In the present work, this model was modified to account for the viscoplastic behaviour of the fluids through a different definition of the Reynolds number, and compared with experimental results.

2 Experimental method

Viscoplastic fluids were prepared by dispersing Carbopol 940 powder (Lubrizol, true density: $\rho = 1400$ kg/m^3) into de-ionised water (Barnstead Easypure); aqueous NaOH solution (30% w/w) was then used to neutralise the Carbopol dispersions[24,25]. Fluids with three different concentrations of Carbopol (Ca 0.067%, 0.079% and 0.1% w/w, respectively) were prepared in order to study the effect of large variations of the yield stress on drop impact behaviour. Viscosities of the model viscoplastic fluids were measured using a rotational rheometer (TA Instruments AR 1000) with a parallel plate geometry (diameter: 40 mm) with rough surfaces to avoid wall slip artefacts. To identify the yield stress, viscosity data obtained for shear stresses above the yield point were fitted with the Herschel-Bulkley (H-B) model, following the well-established procedure[25].

$$\tau = \tau_0 + k\dot{\gamma}^n. \quad (1)$$

where τ is the shear stress, τ_0 the yield stress, $\dot{\gamma}$ the shear rate, k the consistency index, and n the flow index. The resulting yield stress values for Carbopol solutions of different concentrations were shown in Table 1, which is consistent with values reported in the reference literature[25].

Recent works suggest Carbopol dispersions may exhibit anomalous time-dependent behaviours departing significantly from the Herschel–Bulkley model[26–30], however these phenomena are still under debate and require further investigation. Therefore we adhere to one of the established fluid characterisation procedures.

Table 1 Properties of model viscoplastic fluids

Ca	0.067%	0.079%	0.1%
Yield stress (Pa)	1.13	3.64	11.7
Surface tension (mN/m)	66	66	66
Density ($\times 10^3$ kg/m^3)	1	1	1
Equilibrium drop diameter (mm)	3.04±0.08	2.99±0.04	2.95±0.12

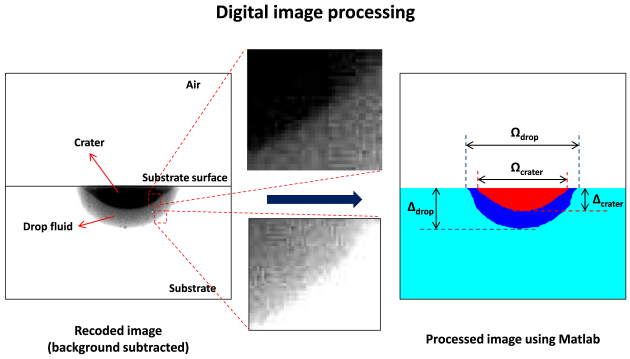

Fig. 2 Schematic of the digital image processing: background-subtracted image (left); processed image using self-developed Matlab code (right).

The experimental setup is conceptually similar to those used in previous drop impact studies[8,10,31]. Drops were released from a blunt hypodermic needle (gauge 21, i.d. 0.495 mm) and impacted on a viscoplastic fluid layer contained in a cubic transparent plastic box (10cm×10cm×10cm). Drop weight measurements made with a precision balance (Mettler PM 100) allowed calculation of the drop diameter at equilibrium, $D_0 = \sqrt[3]{6m/(\pi\rho)}$. Values of equilibrium drop diameters were obtained from averages over 50 samples (see Table 1). The depth of the liquid substrate was always set to 1 cm since in preliminary experiments it was found that the substrate depth had negligible effect on the morphology of drop impact if the depth was more than three times the equilibrium drop diameter. Adjusting the position of the dispensing needle with a digital height gauge allowed changing the impact velocity hence the impact Weber number, $We = \rho D_0 u_i^2/\sigma$, which expresses the competition between kinetic energy and surface energy. For falling heights smaller than 15 cm, the impact velocity is almost identical to the theoretical free fall velocity, $u_i = \sqrt{2g(H_0 - D_0)}$[31], so that the Weber number can be calculated as

$$We = 2g\rho D_0(H_0 - D_0)/\sigma. \quad (2)$$

A systematic investigation on the measurements of the surface tension of viscoplastic fluids by Boujlel et al. showed that Carbopol gels appear to have almost the same value (0.066 N/m) of surface tension irrespective of their yield stress, but this value is only about 10% smaller than that of pure water at ambient temperature[32]. This value of the surface tension of Carbopol gels is used in the calculation of Weber number in the present work since our experiments were conducted at controlled ambient temperature of 20 °C.

The impacts of single drops were recorded using a high-speed CMOS camera (Phantom v9000) at the rate of 4000 frames per second; this yields an uncertainty on time, and in particular on the impact time, t_0, of ±0.125 ms. The camera was horizontally aligned with the impact surface in order to measure the dimensions of both drop fluid and crater with precision. Corrections of measured data were properly made by considering the magnification change due to the variation of the refraction index (from the substrate, through the plastic wall, to the air). Back-to-front illumination was provided by an LED lamp (Philips Accent LED), which ensured a uniform intensity in the field of view. Drops were dyed with 0.1% (w/w) black ink in order to distinguish the drop fluid from the substrate/crater; the effect oof the dye on the fluid yield stress and surface tension was negligible.

Drop impact movies were analysed by digital image processing in two stages: in the first stage, the background is subtracted from each frame and the image brightness, contrast, gamma correction, and digital gain were adjusted manually in order to get clear profiles of both the crater and the drop fluid, represented by the dark and grey regions in the left part of Figure 2, respectively. In the second stage, the image is processed further to capture both the profiles of the crater and the drop fluid through basic image segmentation algorithms; in particular, boundaries were identified as the lines corresponding to maximum intensity gradients as shown by the close-ups in Figure 2. Three different colours are used to denote different regions (red: crater; dark blue: drop; & light blue: substrate). The measurements of the crater dimensions (Ω_{crater}, Δ_{crater}) and drop fluid dimensions (Ω_{drop}, Δ_{drop}) can be easily obtained from the processed image displayed in the right part of Figure 2.

3 Results and Discussion

3.1 Morphology

The impact morphology of viscoplastic drops onto viscoplastic substrates is shown in Figure 3. In particular, six cases are selected: (a) an impacting drop with yield stress $\tau_0 = 1.13$ Pa on substrate with the same yield stress at impact Weber number 15; (b) an impacting drop with yield stress $\tau_0 = 1.13$ Pa on substrate with the same yield stress at impact Weber number 85; (c) an impacting drop with yield stress $\tau_0 = 3.64$ Pa on substrate with the same yield stress at impact Weber number 15; (d) an im-

pacting drop with yield stress $\tau_0 = 3.64$ Pa on substrate with the same yield stress at impact Weber number 85; (e) an impacting drop with yield stress $\tau_0 = 1.13$ Pa on substrate with $\tau_0 = 3.64$ Pa at impact Weber number 50; (f) an impacting drop with yield stress $\tau_0 = 3.64$ Pa on substrate with $\tau_0 = 1.13$ Pa at impact Weber number 50. From these image sequences the common feature of the morphology of a viscoplastic drop impacting on a viscoplastic substrate can be summarized: first, the drop fluid penetrates the substrate with an approximately hemispherical shape; second, a crater is developed due to the large kinetic energy of the impacting drop which deforms the free surface; last, the crater retracts due to the combined effects of buoyancy and surface energy minimisation and finally disappears, however some of the drop fluid remains permanently nestled into the substrate (see the last two images for each case).

Although the interface between the gel substrate and air is of difficult interpretation, both because of the change in the refractive index and because of some blurring due to background subtraction, one can observe capillary waves[33] propagating in the radial direction from the impact point. Previous studies showed that viscoplastic drops may have highly non-spherical shapes prior to impact[4,6,8], which may affect significantly the crater evolution; however the relatively low yield stresses of the fluids used in the present work ensure the drop shape before impact is spherical irrespective of the Weber number, as shown in Figure 4 (note that the optical system is focused on the drop profile below the surface so the drop profile above the liquid surface is less sharp).

The morphology of a softer drop impacting on a harder surface is compared with that of a harder drop impacting on a softer surface at the same impact Weber number in Figures 3e and 3f. The initial development is almost identical. However a larger crater is formed for the case of harder-drop/softer-surface combination due to the softness of the surface which leads to greater deformation. The final shape at the end of impact becomes asymmetric compared to the softer-drop/harder-surface case (note this asymmetry is observed systematically in repeated experiments).

Figure 5 plots the temporal variations of the normalised dimensions (Δ & Ω) with respect to equilibrium drop diameter of both the drop fluid and the crater for four different cases. An almost linear increase of the depth of both the crater and the drop fluid with respect to time is observed in the initial stage for all cases. The growth rate of the crater depth is higher than that of the drop fluid in case of low Weber numbers (Figure 5a & Figure 5b) whilst the growth rates are almost the same at high impact We numbers (Figure 5c & Figure 5d). A systematic comparison between the experimental data and the prediction of crater evolution model for Newtonian drops by Bisighini. et al.[20] will be discussed in the following sections.

An interesting phenomenon observed here is the permanent nestling of the drop fluid in the substrate under the impact point.

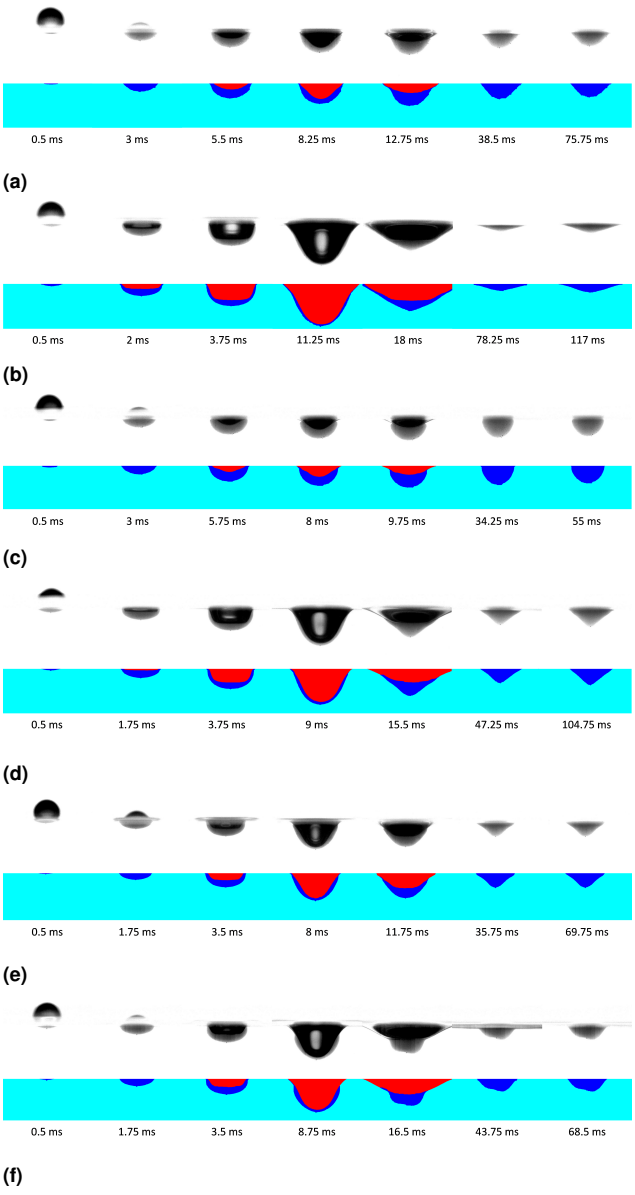

Fig. 3 Impact morphology of viscoplastic drops onto gel substrates: (a) drop ($\tau_0 = 1.13$ Pa), substrate ($\tau_0 = 1.13$ Pa) & $We = 15$; (b) drop ($\tau_0 = 1.13$ Pa), substrate ($\tau_0 = 1.13$ Pa) & $We = 85$; (c) drop ($\tau_0 = 3.64$ Pa), substrate ($\tau_0 = 3.64$ Pa) & $We = 15$; (d) drop ($\tau_0 = 3.64$ Pa), substrate ($\tau_0 = 3.64$ Pa) & $We = 85$; (e) drop ($\tau_0 = 1.13$ Pa), substrate ($\tau_0 = 3.64$ Pa) & $We = 50$; (f) drop ($\tau_0 = 3.64$ Pa), substrate ($\tau_0 = 1.13$ Pa) & $We = 50$. The first row displays original images and the second row the same images after processing; the time after impact is indicated at the bottom.

The drop fluid remains confined within a volume with either conical, irregular, or spherical-cap shape, which is preserved in time

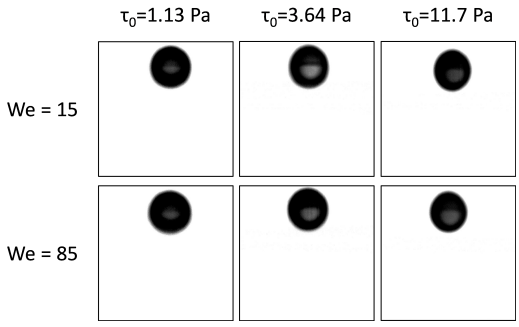

Fig. 4 Drop shapes before impact. Impact Weber number We=15 & 85..

due to the intrinsic yield-stress nature of both the drop and the substrate, which reduces significantly molecular diffusion and advection in comparison with low-viscosity Newtonian fluids. The final shape of a drop deposited onto a partially cured substrate is of great importance in the inkjet manufacturing process. For this reason, the final profiles of the impacting drops for different drop/surface yield stress combinations and different Weber numbers ($We = 15,\ 50\&85$) are displayed in Figure 6. One can observe that the final shape of the impacting drops has is approximately a spherical cap at low Weber numbers, but tends to evolve into a conical or truncated-conical shape as the Weber number increases for all combinations of drop/substrate yield stresses.

The depth of the impacting drop grows with the Weber number for drop impacts on harder substrate ($\tau_0 = 11.7$ Pa), however for softer substrates (e.g., $\tau_0 = 1.13$ Pa) the impacting drop expands horizontally instead of penetrating vertically at high impact Weber numbers. As a consequence, in the case of softer substrates the penetration depth of the impacting drop surprisingly decreases with respect to the increase of the Weber number, as shown in Figure 7, which plots the depth of final profiles of impacting drops as a function of the yield stress at three different Weber numbers. The experimental data averaged over five experiments per set are divided into three groups according to the stiffness of the substrate (soft: $\tau_0 = 1.13$ Pa in Figure 7a, intermediate :$\tau_0 = 3.64$ Pa in Figure 7b and hard: $\tau_0 = 11.7$ Pa in Figure 7c). As shown in Figure 7, the depth of the impacting drop increases monotonically as the drop becomes harder (i.e. higher yield stress) except in the case of the intermediate substrate at $We = 85$, which does not show significant changes.

3.2 Volume of final shape

The volume of the final shape of the drop fluid underneath the surface of the substrate can be estimated through the digital information extracted from the processed images (Figure 3) at the end of impact. Under the assumption that the final shape is axisymmetric, the total volume of the depositing drop material below the substrate surface can be calculated from the sum of the volumes of several thin disks as shown in Figure 8. The integral expression of the total volume can be discretized by the sum of

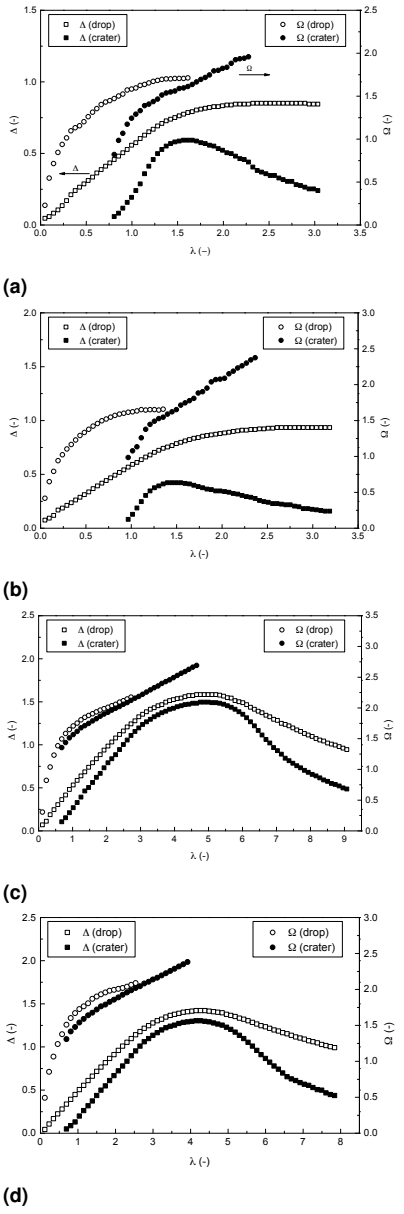

Fig. 5 The normalised dimensions (Δ & Ω) of both drop fluid (open symbols) and crater (filled symbols) as a function of dimensionless time (λ) for four different cases: (a) $\tau_{0,drop} = 1.13$ Pa, $\tau_{0,substrate} = 1.13$ Pa, $We = 15$; (b) $\tau_{0,drop} = 3.64$ Pa, $\tau_{0,substrate} = 3.64$ Pa, $We = 15$; (c) $\tau_{0,drop} = 1.13$ Pa, $\tau_{0,substrate} = 1.13$ Pa, $We = 85$; (d) $\tau_{0,drop} = 3.64$ Pa, $\tau_{0,substrate} = 3.64$ Pa, $We = 85$.

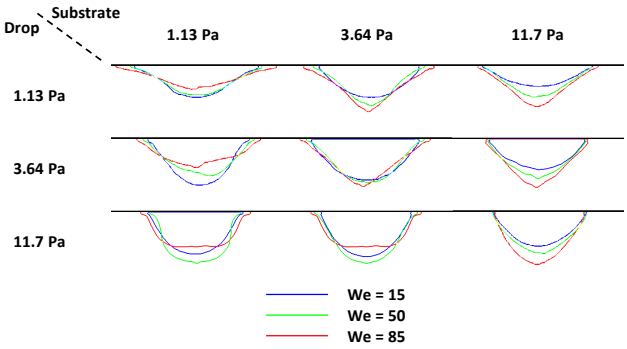

Fig. 6 The morphology map of impacting drops for different drop/substrate combinations at low (We=15, blue line), intermediate (We=50, green line) and high (We=85, red line) Weber numbers. The top row indicates the yield stress values of the substrate while the column on the left denotes the values of impacting drops.

finite small disks with thickness of one pixel:

$$V_{\text{final}} = \int_0^{X_{\text{depth}}} \mathrm{d}V = \int_0^{X_{\text{depth}}} \frac{\pi D^2(x)}{4} \mathrm{d}x \approx \sum_{i=1}^{n} \frac{\pi D^2(i)}{4} \Delta x, \qquad (3)$$

where $D(i)$ denotes the local diameter of the disk measured by image processing, Δx the thickness of the disk (size of one pixel) and n the number of disks.

The ratio of this quantity to the original volume of the drop released from the needle (V_{final}/V_0) can be used as an indicator of the degree of penetration or diffusion. For a case of $V_{\text{final}}/V_0 < 1$, the drop partially penetrates the substrate leaving a part of the original fluid material over the surface of the substrate (a bump over the substrate surface is observed). However if $V_{\text{final}}/V_0 \approx 1$, it is suggested all the drop material is immersed in the substrate (i.e. full penetration), which which occurs when the apparent drop volume (calculated from the grey region, see Figure 2) is almost the same as the volume of the original drop. This quantity is closely related to two parameters: (i) the impact Weber number ($We = \rho D_0 u_i^2/\sigma$); (ii) the ratio of the yield stress magnitude of the drop to that of the substrate ($\beta = \tau_{0,\,\text{drp}}/\tau_{0,\,\text{sub}}$). The former expresses the magnitude of kinetic energy carried by the impacting drop since the surface tension is approximately the same for all model fluids (Table 1). The latter indicates the relative stiffness of the impacting drop compared to the substrate. At higher impact Weber numbers, a high value of V_{final}/V_0 is expected due to the large crater formation induced by high kinetic energy. Since the substrate is more likely to deform if the relatively stiffness of the drop is higher, it is anticipated that V_{final}/V_0 grows as the yield stress ratio, β, increases.

Figure 9 shows the normalized drop volume beneath the surface as a function of the yield stress ratio at different impact Weber numbers. These data suggest the amount of drop fluid penetrated into the substrate increases as a function of the yield stress ratio; this becomes more evident when data correspond-

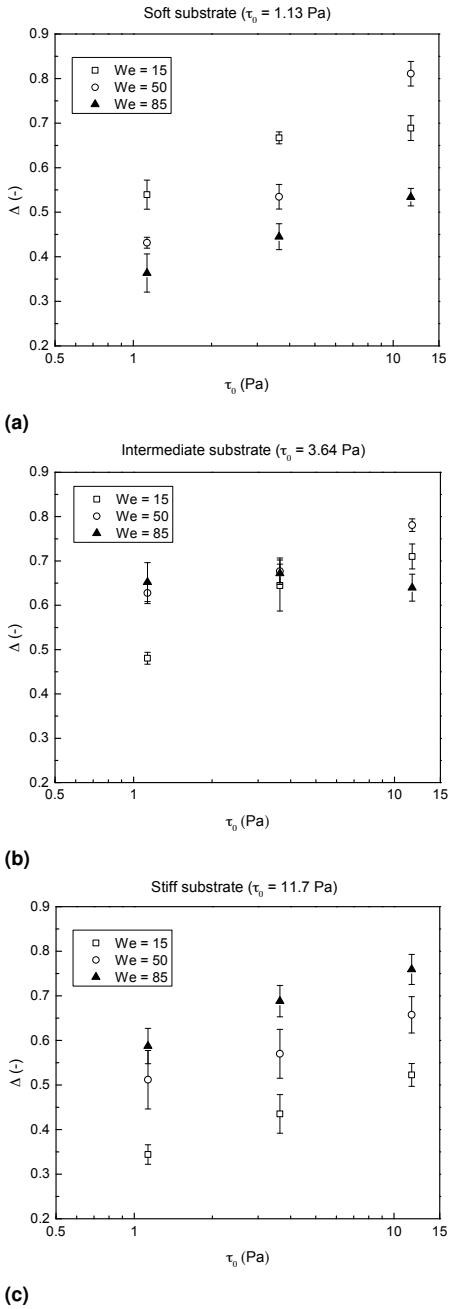

Fig. 7 Depth of final profiles of impact drops as a function of the yield stress of impacting drops at three different Weber numbers: (a) soft substrate ($\tau_0 = 1.13$ Pa); (b) intermediate substrate ($\tau_0 = 3.64$ Pa); (c) stiff substrate ($\tau_0 = 11.7$ Pa).

ing to drop/substrate combinations with similar values of β (e.g. the combination with $\tau_{0,\,\mathrm{drp}}/\tau_{0,\,\mathrm{sub}} = 1.13/3.64 \approx 0.310$ and the combination with $\tau_{0,\,\mathrm{drp}}/\tau_{0,\,\mathrm{sub}} = 3.64/11.7 \approx 0.311$) are grouped together, as shown in Figure 10. The horizontal dashed line is provided as a guide to the eye to distinguish the 'full penetration' ($V_{\mathrm{final}}/V_0 \approx 1$) regime and the 'partial penetration' ($V_{\mathrm{final}}/V_0 < 1$) regime. As expected, V_{final}/V_0 increases monotonically with respect to both We and β, therefore this quantity can be conveniently re-plotted as a function of a single dimensionless parameter, i.e. the product (βWe); the experimental data of normalized drop volume as a function of βWe is plotted in Figure 11. Considering a function representing these experimental data $V_{\mathrm{final}}/V_0 = f(\beta We)$ with the following asymptotic properties, $\lim_{\beta We \to 0} V_{\mathrm{final}}/V_0 = 0$ and $\lim_{\beta We \to \infty} V_{\mathrm{final}}/V_0 = 1$, one can propose an empirical correlation:

$$V_{\mathrm{final}}/V_0 = \frac{1}{1 + m(\beta We)^{-n}}, \tag{4}$$

where m and n are constants obtained from least-squares fitting, and their numerical values are $m = 1.2$ & $n = 0.82$, with a correlation coefficient 0.92.

3.3 Crater evolution

Experimental data are compared with the prediction of a crater evolution model developed for Newtonian fluids[20]. Since the model assumes the same fluid for the drop and the impact surface, only the drop/substrate combinations with the same yield stress are considered. The temporal evolution of the dimensionless diameter (or width), Ω, during the initial stage can be approximated as:

$$\Omega \approx 2\sqrt{(\alpha_0 + 0.17\lambda)^2 - (0.27\lambda - \alpha_0)^2}, \tag{5}$$

where λ is the dimensionless time and α_0 a constant associated with the initial cavity radius. Measurements of the temporal evolution of the crater and drop fluid diameters in the initial stage reported in Figure 5 above were fitted to Equation 5 separately,

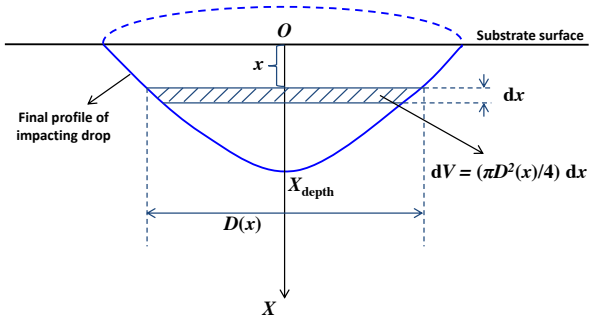

Fig. 8 Schematic of the volume calculation of drop fluid.

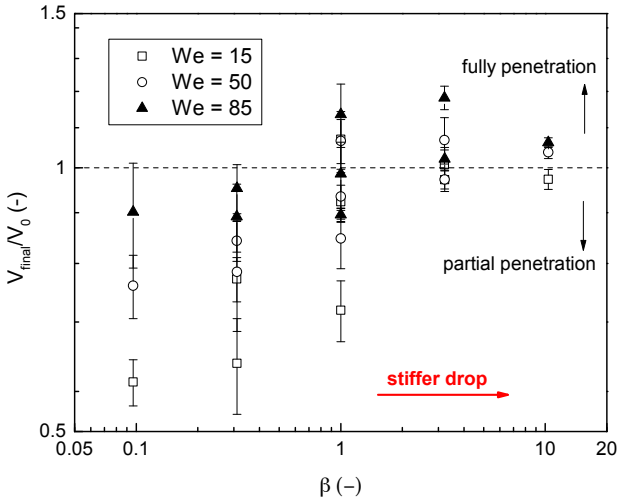

Fig. 9 Normalized drop volume beneath the surface as a function of β at different impact Weber numbers.

as shown in Figure 12 (note dimensionless time is used). Fitting experimental data relative to Newtonian fluids using the same model yields a constant $\alpha_0 = 0.77$[20]. Here, a constant $\alpha_0 = 0.71$ with standard error 0.011 (Figure 12a) was obtained for the temporal evolution of drop fluid diameter, while a value $\alpha_0 = 0.85$ with standard error 0.027 (Figure 12b) for the crater diameter evolution. Thus, the model is in better agreement with the drop fluid diameter rather than the crater diameter.

In the crater evolution model, the dimensionless depth grows linearly with respect to dimensionless time in the initial stage ($\lambda < \lambda^*$):

$$\Delta = 0.44\lambda. \tag{6}$$

In the second stage ($\lambda > \lambda^*$) the crater evolution for inviscid flow can be described by the following differential equations (where $\Delta = \alpha + \zeta$):

$$\ddot{\alpha} = -\frac{3}{2}\frac{\dot{\alpha}^2}{\alpha} - \frac{2}{\alpha^2 We} - \frac{1}{Fr}\frac{\zeta}{\alpha} + \frac{7}{4}\frac{\dot{\zeta}^2}{\alpha}, \tag{7}$$

$$\ddot{\zeta} = -3\frac{\dot{\alpha}\dot{\zeta}}{\alpha} - \frac{9}{2}\frac{\dot{\zeta}^2}{\alpha} - \frac{2}{Fr}. \tag{8}$$

Viscous effects can be taken into account by introducing the viscous energy dissipation terms into Equation 7 and Equation 8:

$$\ddot{\alpha} = -\frac{3}{2}\frac{\dot{\alpha}^2}{\alpha} - \frac{2}{\alpha^2 We} - \frac{1}{Fr}\frac{\zeta}{\alpha} + \frac{7}{4}\frac{\dot{\zeta}^2}{\alpha} - \frac{4\dot{\alpha}}{\alpha^2 Re}, \tag{9}$$

$$\ddot{\zeta} = -3\frac{\dot{\alpha}\dot{\zeta}}{\alpha} - \frac{9}{2}\frac{\dot{\zeta}^2}{\alpha} - \frac{2}{Fr} - \frac{12\dot{\zeta}}{\alpha^2 Re}. \tag{10}$$

Initial conditions can be obtained from the linear approximation

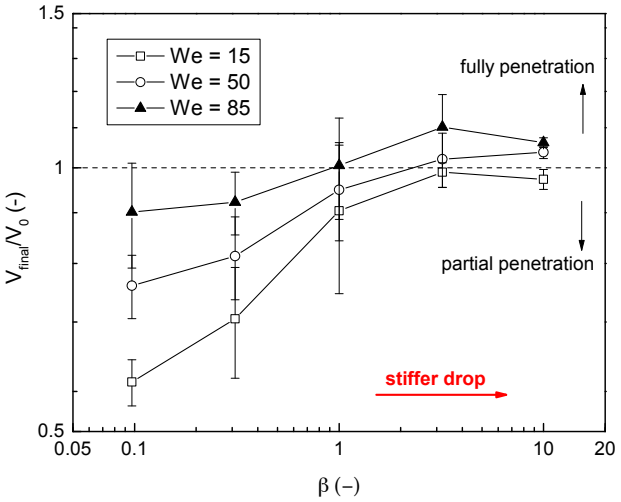

Fig. 10 Normalized drop volume beneath the surface as a function of β at different impact Weber numbers. Data with close values of yield stress ratios are grouped together for clarity.

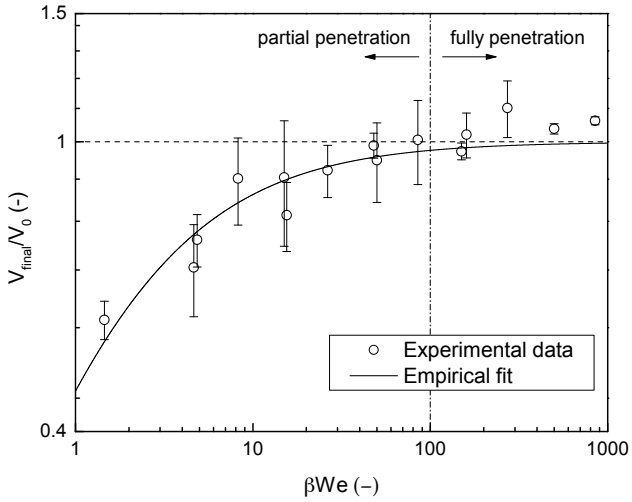

Fig. 11 Normalized drop volume beneath the surface as a function of βWe. Experimental data are represented by open circles while solid line indicates the empirical fit.

in the first stage of impact[20]:

$$\dot{\alpha} \approx 0.17,\ \alpha \approx \alpha_0 + 0.17\lambda,\ \dot{\zeta} \approx 0.27,\ \zeta \approx -\alpha_0 + 0.27\lambda. \qquad (11)$$

The model prediction of the crater evolution can be calculated by numerical integration of the system of ordinary differential Equations 7 and 8 (Equations 9 and 10 if considering viscous effects) using the initial condition from Equation 11 at $\lambda = \lambda^*$. For instance $\lambda^* = 1.3$ is observed for the case of the evolution of drop fluid in Figure 5a. Together with $\alpha_0 = 0.72$ obtained from the diameter evolution model fit for drop fluid (Figure 12a), the initial condition for this case can be calculated as: $\dot{\alpha}(1.3) = 0.17,\ \alpha(1.3) = 0.941,\ \dot{\zeta}(1.3) = 0.27,\ \zeta(1.3) = -0.369$. The predicted dimensionless depth as a function of dimensionless time is compared with the experimental data for both drop fluid and crater in Figure 13. The Reynolds numbers in Equation 9 and 10 are calculated using the generalized definition of Reynolds number for the flow of a Herschel-Bulkley fluid derived by Madlener et al.[34]:

$$Re_{\mathrm{HB}} = \frac{\rho u_i^{2-n} D_0^n}{(\tau_0/8)(D_0/u_i)^n + K((3m+1)/(4m))^n 8^{n-1}}. \qquad (12)$$

where K and n are flow parameters in Equation 1, u_i the impact velocity and $m = (nK(8u_i/D_0)^n)/(\tau_0 + K(8u_i/D_0)^n)$. As shown in Figure 13a and 13c, the agreement between the experimental data the model prediction for the dimension of the drop fluid is reasonable at least in the first stage. The linear growth predicted by the model (Eq. 6) in the first stage is observed and the maximum depth is also correctly predicted. However for the case of crater dimension (Figure 13b and 13d), the depth grows faster than the model prediction in the first stage at low impact Weber number (see the filled square symbols in Figure 13b and 13d). Also the crater evolution model underpredicts the maximum crater depth at $We = 15$ while at a higher impact Weber number the maximum depth is overpredicted. The discrepancy between the model predictions of inviscid flow and those obtained considering viscous effect is negligibly small, therefore viscous effects do not play a major role in the model, which is not obvious a priori. Nevertheless the fact that the maximum depth for both cases of drop fluid and crater decreases as the yield stress increases indicates the magnitude of yield stress still plays an important role in case of viscoplastic fluids. The overall agreement between the experimental data and model prediction is better when describing the dimension of drop fluid than the crater.

At high impact Weber number, the drop fluid distributes almost uniformly over the large surface of the crater, forming a thin layer; thus, the difference between the dimensions of the crater and those of the drop fluid are negligibly small. For this reason, the crater evolution model is better at predicting the crater evolution at high impact Weber numbers, where the crater and the drop fluid are almost coincident. However, when the impact Weber number is low the drop forms a thick layer, hence there are greater differences between the evolution of the crater and that of the drop fluid. This behaviour was not observed in previous studies using low-viscosity Newtonian fluids, where there is an almost instantaneous mixing of the drop into the liquid substrate.

4 Conclusions

The impact of viscoplastic drops onto viscoplastic substrates characterized by different magnitudes of yield stress was investigated experimentally. The impact morphology of different drop/substrate combinations, with yield stresses ranging from 1.13 Pa to 11.7 Pa, was studied through high speed imaging for impact Weber numbers between 15 and 85. A map showing the final profiles of the impacting drops for different combinations of drops and substrates with different magnitudes of yield stresses at three Weber numbers ($We = 15,\ 50\&85$) was constructed. It was observed that the final profiles of the impacting drops transform from a semicircle (a hemisphere in 3D) to a triangle (a cone in 3D) as the Weber number increases for all combinations. Also the magnitude of the yield stress of the substrate strongly affected the penetration depth of drop fluid: depth increases as the impact Weber number grows for stiff surface while decreases for soft surface. The volumes of the final shapes for different impact parameters were calculated through image processing. A single dimensionless parameter was introduced by the product of drop/substrate yield stress ratio and Weber number (βWe) to reduce the regime map of behaviour from two parameters to one. Experimental data of the temporal crater evolution were fitted to one of the existing models on crater evolution. The comparison between experimental data and model prediction implies the crater evolution model is more suitable to describe the dimension of the drop fluid rather than the crater.

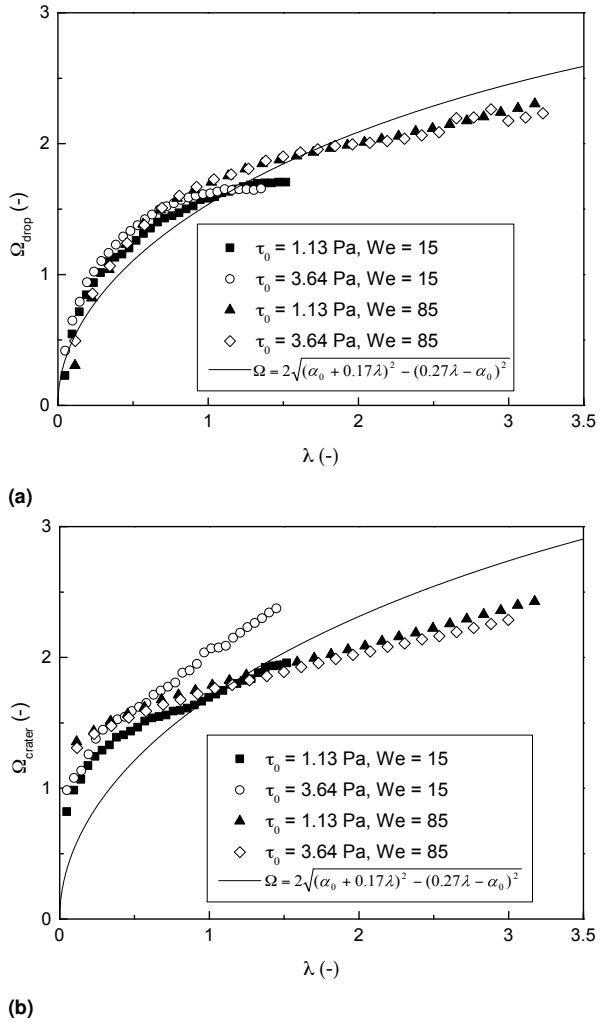

Fig. 12 Temporal evolution of the dimensionless diameter of drop/crater for different impact parameters and the fit curve by crater evolution model: (a) drop fluid; (b) crater.

References

1 P. Coussot, *Soft Matter*, 2007, **3**, 528–540.
2 N. J. Balmforth, I. A. Frigaard and G. Ovarlez, *Annual Reviews of Fluid Mechanics*, 2014, **46**, 121–146.
3 P. Coussot and F. Gaulard, *Physical Review E*, 2005, **72**, 031409.
4 G. German and V. Bertola, *Physics of Fluids*, 2010, **22**, 033101.
5 L. Hermany, D. Dall'Onder dos Santos, S. Frey, M. Naccache and P. de Souza Mendes, *Journal of Non-Newtonian Fluid Mechanics*, 2013, **201**, 1–9.
6 G. German and V. Bertola, *Journal of Non-Newtonian Fluid Mechanics*, 2010, **165**, 825–828.
7 S. Nigen, *Atomization and Sprays*, 2005, **15**, 103–117.
8 G. German and V. Bertola, *Journal of Physics: Condensed Matter*, 2009, **21**, 375111.
9 G. German and V. Bertola, *Colloids and Surfaces A: Physicochemical and Engineering Aspects*, 2010, **366**, 18–26.
10 S. Chen and V. Bertola, *Soft Matter*, 2016, **12**, 7624–7631.
11 V. Bertola, *Journal of Physics: Condensed Matter*, 2009, **21**, 035107.
12 M. Jalaal, N. J. Balmforth and B. Stoeber, *Langmuir*, 2015, **31**, 12071–12075.
13 B. C. Blackwell, M. E. Deetjen, J. E. Gaudio and R. H. Ewoldt, *Physics of Fluids*, 2015, **27**, 043101.
14 S. Tavangar, S. H. Hashemabadi and A. Saberimoghadam, *Fuel Processing Technology*, 2015, **132**, 153–163.
15 A. Maleki, S. Hormozi, A. Roustaei and I. Frigaard, *Journal of Fluid Mechanics*, 2015, **769**, 482–521.
16 C. Xie, J. Zhang, V. Bertola and M. Wang, *Journal of Non-Newtonian Fluid Mechanics*, 2016, **234**, 118–128.
17 L. J. Leng, *Journal of Fluid Mechanics*, 2001, **427**, 73–105.
18 A. I. Fedorchenko and A.-B. Wang, *Physics of Fluids*, 2004, **16**, 1349–1365.

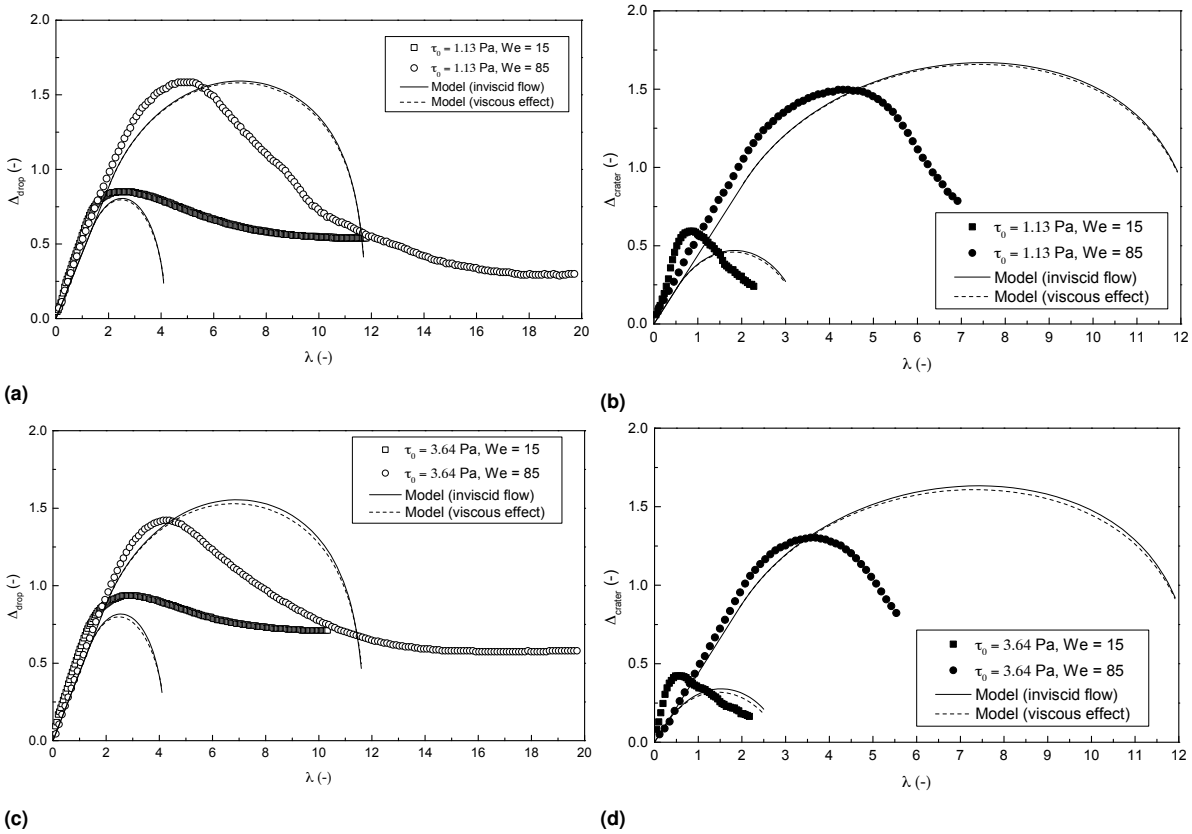

Fig. 13 The dimensionless depth of crater/drop as a function of dimensionless time at various impact parameters: (a) dimension of drop fluid, $\tau_0 = 1.13$ Pa; (b) dimension of crater, $\tau_0 = 1.13$ Pa; (c) dimension of drop fluid, $\tau_0 = 3.64$ Pa; (d) dimension of crater, $\tau_0 = 3.64$ Pa. The experimental data are represented by symbols. Solid lines indicate the model prediction for inviscid flow while the dashed lines show the difference if viscous effect is taken into account.

19 M. H. Hendrix, W. Bouwhuis, D. van der Meer, D. Lohse and J. H. Snoeijer, *Journal of fluid mechanics*, 2016, **789**, 708–725.

20 A. Bisighini, G. E. Cossali, C. Tropea and I. V. Roisman, *Physical Review E*, 2010, **82**, 036319.

21 R. L. Vander Wal, G. M. Berger and S. D. Mozes, *Experiments in Fluids*, 2006, **40**, 33–52.

22 T. Okawa, T. Shiraishi and T. Mori, *Experiments in Fluids*, 2008, **44**, 331–339.

23 X. Chen, S. Mandre and J. J. Feng, *Physics of Fluids*, 2006, **18**, 092103.

24 S. Curran, R. Hayes, A. Afacan, M. Williams and P. Tanguy, *Journal of food science*, 2002, **67**, 176–180.

25 G. P. Roberts and H. A. Barnes, *Rheologica Acta*, 2001, **40**, 499–503.

26 A. Putz and T. Burghelea, *Rheologica Acta*, 2009, **48**, 673–689.

27 E. Weber, M. Moyers-González and T. Burghelea, *Journal of Non-Newtonian Fluid Mechanics*, 2012, **183–184**, 14–24.

28 T. Divoux, V. Grenard and S. Manneville, *Physical Review Letters*, 2013, **110**, 018304.

29 R. Sainudiin, M. Moyers-González and T. Burghelea, *Soft Matter*, 2015, **11**, 5531–5545.

30 A. Poumaere, M. Moyers-González, C. Castelain and T. Burghelea, *Journal of Non-Newtonian Fluid Mechanics*, 2014, **205**, 28–40.

31 V. Bertola, *International journal of heat and mass transfer*, 2009, **52**, 1786–1793.

32 J. Boujlel and P. Coussot, *Soft Matter*, 2013, **9**, 5898–5908.

33 M. Rein, *Physics of Fluids*, 2002, **14**, 411–414.

34 K. Madlener, B. Frey and H. Ciezki, Progress in Propulsion Physics, 2009, pp. 237–250.